ELSEVIER

Contents lists available at ScienceDirect

Journal of the European Ceramic Society

journal homepage: www.elsevier.com/locate/jeurceramsoc





Blacklight sintering of garnet-based composite cathodes

Walter Sebastian Scheld ^{a,b,*}, Julian N. Ebert ^a, Michael Scherer ^c, Lovro Fulanovic ^c, Lukas Porz ^c, Christian Dellen ^a, Martin Ihrig ^a, Sven Uhlenbruck ^a, Martin Finsterbusch ^a, Olivier Guillon ^{a,d,e}, Dina Fattakhova-Rohlfing ^{a,b,*}, Wolfgang Rheinheimer ^{a,e}

- a Forschungszentrum Jülich GmbH, Institute of Energy and Climate Research, Materials Synthesis and Processing IEK-1, 52425 Jülich, Germany
- ^b University of Duisburg-Essen, Faculty of Engineering and Center for Nanointegration Duisburg-Essen CENIDE, Lotharstraβe 1, 47057 Duisburg, Germany
- ^c Department of Materials and Earth Sciences, Technical University of Darmstadt, Peter-Grünberg-Straβe 2, 64287 Darmstadt, Germany
- ^d Jülich Aachen Research Alliance JARA-ENERGY, 52425 Jülich, Germany
- ^e Institute of Mineral Engineering, RWTH Aachen University, 52064 Aachen, Germany

ARTICLE INFO

Keywords: Xe flash lamp annealing Photonic sintering Li solid-state battery Ceramic Li₇La₃Zr₂O₁₂ LiCoO₂ Garnet LLZO LCO Energy storage Composite cathode

ABSTRACT

Garnet-structured $\text{Li}_7\text{La}_3\text{Zr}_2\text{O}_{12}$ (LLZO) is an attractive electrolyte for lithium solid-state batteries (SSBs), but its processing requires long sintering at temperatures above $1000\,^{\circ}\text{C}$ to achieve sufficient ionic conductivity. Such sintering is not only time and energy consuming, but also leads to undesirable material interactions. Therefore, a significant reduction of the sintering time is very important for the future development of garnet-based batteries. A promising method is the recently introduced photonic blacklight sintering with light sources in the UV spectrum, which enables energy-efficient sintering of ceramic layers within seconds. In this work, blacklight sintering of garnet-based SSBs is validated using a model cell consisting of LLZO and LiCoO₂ (LCO) composite cathode layers printed on dense LLZO pellets. An optimized sintering program allowed the production of working cells in only 20 s. This study demonstrates the suitability of blacklight sintering for processing garnet-based SSBs and provides guidance for future process optimization.

1. Introduction

Solid-state batteries (SSB) with solid electrolytes (SE) are a promising technology that could outperform Li-ion batteries (LIB) in terms of energy density and, most importantly, safety [1]. The garnet type ${\rm Li}_7{\rm La}_3{\rm Zr}_2{\rm O}_{12}$ (LLZO) is one of the intensively studied SEs due to its moderate high ionic conductivity of up to 2 S cm $^{-1}$ at room temperature, its wide electrochemical stability window, compatibility with Li metal, non-flammability, and its wide operating temperature range [2,3]. However, due to its oxide ceramic nature, LLZO requires a densification step, which is usually achieved by sintering at high temperatures of > 1000 °C [4–8]. The high sintering temperatures activate ion diffusion to form sintering necks required for ionic conductivity, but also lead to undesirable interfacial reactions. In particular, the processes at the interface between the cathode active material (CAM) and LLZO during sintering of ceramic composite cathodes are known to lead to several detrimental effects that deteriorate battery performance, which will be

discussed in more detail later [9–22]. Another important aspect of the sintering process is energy consumption, which depends drastically on the sintering method. Conventional high-temperature processes for sintering LLZO ceramic powders into solids, which are performed for several hours at a temperature below the melting point, driven by a reduction in surface energy, are the most energy-intensive production steps [23–27]. During the long heating times, almost all energy is lost through heat losses via insulation and ventilation [28,29]. Therefore, the sintering step offers great potential for reducing energy demand through the use of more efficient technologies [30–32].

To reduce the energy consumption and undesirable material interactions, finding new processing techniques with much shorter sintering times is a necessary technological step. Examples of advanced sintering techniques include microwave sintering, flash sintering, field-assisted sintering/spark plasma sintering (FAST/SPS), rapid thermal processing (RTP), ultrafast high-temperature sintering (UHS), laser sintering, and flash lamp sintering [8,30,33–37]. LCO-LLZO-based SSBs

E-mail addresses: s.scheld@fz-juelich.de (W.S. Scheld), d.fattakhova-rohlfing@fz-juelich.de (D. Fattakhova-Rohlfing).

^{*} Corresponding authors at: Forschungszentrum Jülich GmbH, Institute of Energy and Climate Research, Materials Synthesis and Processing IEK-1, 52425 Jülich, Germany.

have already been successfully fabricated using RTP [35,36], laser sintering [38,39], FAST/SPS [14,40], and UHS [41]. Still, these techniques have several limitations or drawbacks that make it difficult to implement a sintering process that combines speed, simplicity, versatility, efficiency, and scalability for large-scale industrial production [42].

However, this could change with the photonic blacklight sintering method reported by Porz *et al.* in 2022 [42]. This process uses a Xe flash lamp with a wavelength in the visible and UV spectrum to heat the entire sample at once with a series of millisecond-long pulses using temperature-dependent electromagnetic wave absorption [42–44]. In this way, a scalable and non-contact sintering process in the time scale of seconds has been achieved that does not require complex equipment and has much lower energy consumption compared to conventional methods [42].

Similar to RTP and laser sintering, blacklight flash lamp sintering is a photonic sintering process that enable fast and easy processing in the short time of seconds [45]. Blacklight flash lamp sintering is faster than the RTP process, which is in the range of minutes, and just as fast as laser sintering, which allows sintering in seconds. The added advantage of blacklight flash lamp sintering over laser sintering is that it heats the entire sample surface at once, as opposed to scanning a focused laser beam across the sample surface [35,36,38,45]. A flash lamp sintering process using a constant radiation source, can be influenced by the intensity of the radiation and the duration of the irradiation. In pulse mode, the pulse length, the number of pulses, and the break time between two pulses can be used to adjust the sintering conditions. The break times between pulses can be used to give the system time to thermally relax to avoid cracking and overheating and to sinter deeper layers, which is especially important for thicker layers. Heat transfer to the substrate and the atmosphere and the sintering atmosphere itself are two other parameters. Since the energy transfer during sintering strongly depends on the radiation absorption and thermal conductivity of the materials, the process parameters have to be adapted to the specific materials. Since the combination of sintering parameters is practically unlimited, the relative effect of important parameters on sintering performance and possible material degradation should be estimated in order to choose a perspective process window, which was the focus of the present work.

To test the suitability of blacklight photonic sintering for processing garnet-based SSBs, composite cathodes, containing LLZO and $\rm LiCoO_2$ (LCO), were printed on dense LLZO pellets (separator) and then sintered using a multi-pulse Xe flash lamp. Pulse length and number of pulses were varied to find suitable sintering parameters. The sintered half-cells were assembled into full cells by attaching indium foils as anode. The microstructure, phase composition, and electrochemical properties of the cathodes were analyzed to establish processing parameters for blacklight sintering of garnet-based cells and to provide guidance for future optimization of this processing method.

2. Experimental

2.1. LLZO synthesis

Ta- and Al- substituted LLZO (Li $_{6.45}$ Al $_{0.05}$ La $_{3}$ Zr $_{1.6}$ Ta $_{0.4}$ O $_{12}$) powder was synthesized with a three-step solid-state reaction (850 °C and 1000 °C for 20 h, and 1175 °C for 10 h) from the educts LiOH $_{12}$ O (APPLICHEM, 99.00%, excess of 10 mol%), La $_{2}$ O $_{3}$ (Merck, 99.90%), ZrO $_{2}$ (Treibacher, 99.70%), Ta $_{2}$ O $_{5}$ (Treibacher, 99.99%), and Al $_{2}$ O $_{3}$ (Inframat, 99.82%). The resulting sintered pellets with a diameter of around 11.15 mm were cut into pieces with a thickness of around 400 $_{\mu}$ m. More information about the LLZO synthesis can be found elsewhere [5–7].

2.2. Composite cathode fabrication

Commercial LCO powder (MTI Corporation, battery grade) was mixed and milled (5 times 750 rpm for 5 min, Ø 5 mm ZrO $_2$ balls) with

powder of the synthesized LLZO (60 wt% LCO: 40 wt% LLZO) in a microplanetary mill (Pulverisette 7, Fritsch) with 2-propanol (Alfa Aesar, 99.5%). The resulting powder mixture was dried and combined with a solution of an isomeric mixture of terpineol (Sigma-Aldrich, 99.50%) and 6 wt% ethyl cellulose (Sigma-Aldrich, 46 cps, 48.00%) in a three-roll mill (50 l, Exakt). The fabricated ink (solid loading of 55 wt%) was printed on the previously cut LLZO discs by screen-printing (E2, Ekra) with a polyester screen (27–120 \times 22.5°, Koenen). Further information about the composite cathode fabrication was published before [35].

2.3. Multi-pulse Xe flash lamp processing

Flash lamp experiments were performed with a multi-pulse Xe flash lamp system (Heraeus Noblelight Ltd) operated at 220 V. For the sintering, a multi-pulse mode was used with a flash frequency of 60 Hz and varied pulse lengths and number of pulses. The light was directed to the sample via a quartz block. The samples were placed at room temperature in ambient atmosphere on expandable graphite (GHL, LUH GMBH, density of 90 kg m $^{-3}$ to 140 kg m $^{-3}$) 10 mm below the quartz block.

2.4. Battery cell assembly

The cell assembly was carried out in argon atmosphere. The anode side of the half-cell was polished with SiC paper (1. 800 grit, 2. 1200 grit, 3. 2500 grit, 4. 4000 grit) and subsequently sputtered on both sides to generate a thin Au film (~3 nm on the anode side, ~30 nm on the cathode side). The Au film on the cathode side acts as current collector, while the Au on the anode side increased the adhesion of indium (In) metal on the anode side [14,15]. After that, an In metal foil was manually attached on the Au coated anode side and subsequently heated up to 157 °C until the In was molten. The In anode was covered with a polished Ni plate and the battery cell were placed in an ECC-Combi test cell (EL-Cell®). The full cell had a diameter of around 1.15 cm (A=1.04 cm²) with around 2 ± 0.1 mg of cathode active material, resulting in a theoretical capacity of 0.28 ± 0.01 mAh.

2.5. Characterization

X-ray diffraction (XRD) (D4 ENDEAVOR, BRUKER) was performed between 10° and 80° in Bragg-Brentano geometry. Raman spectroscopy mapping (INVIA Qontor, Renishaw) was performed with a 532 nm laser (\sim 2.5 mW) and a 2400 l mm $^{-1}$ grating. The spectra were collected with a step size of (x, y) = (1 μ m, 1 μ m) over an area of 80 μ m \times 40 μ m with a total number of 3321 spectra and a measuring time of 1 s per spectrum. The spectra were processed with the WiRETM software (Renishaw), including cosmic ray removal, background subtraction, and normalization. Each single spectrum of the Raman mapping were separated by a component analysis to the LLZO or the LCO phase and the resulting sets of spectra were averaged, like in [35]. For microstructural analysis, the samples were coated with a thin sputtered Au layer and analyzed with a scanning electron microscope (SEM) (TM3000, HITACHI) using a backscattered electron (BSE) detector. For cross-section images, the pellets were broken in the middle and polished with SiC paper (1.800 grit, 2. 1200 grit, 3. 2500 grit, 4. 4000 grit) and 1 µm diamond suspension. The electron acceleration voltage was set to 15 kV. Full cell electrochemical tests were carried out in a climate chamber (VT 4002EMC, VÖTSCH Industrietechnik) at a constant temperature of 60 °C with a potentiostat (VMP-300, Biologic). The cell was electrochemically cycled between 2.8 V and 3.6 V vs. Li-In with a constant current of 20 μA (current density of 19.3 $\mu A \text{ cm}^{-2}$ and a C-rate of 0.07 C). In the charging process, the voltage was maintained at 3.6 V vs. Li-In until the current was reduced to 10 µA. Electrochemical impedance spectroscopy (EIS) started after 5 min of open cell voltage (OCV) with a frequency varied from 3 MHz to 100 mHz and an electrical field perturbation of 10 mV.

3. Results and discussion

An optimal design of a garnet-based SSB includes a thin and dense LLZO separator connected to a composite cathode (CAM and LLZO) and a Li metal or Li alloy anode. Since the separator requires higher temperatures than the CAM for full densification, it is usually sintered first, followed by deposition of a composite cathode that can be sintered at lower temperatures to minimize the side effects summarized in Fig. 1, all of which directly affect the cell performance [6,17,21,35,38].

Chemical reactions between LLZO and CAM during co-sintering are one of the biggest challenges in the fabrication of composite cathodes [11-20,46]. Even LCO, which has the highest thermal stability in combination with LLZO, often forms secondary phases such as Li_{0.5}La₂-Co_{0.5}O₄ [15,38], LaCoO₃ [16], La₂CoO₄ [47], La₂Zr₂O₇ [16,17], CoO [36,48], Co_3O_4 [36,48], and La_2O_3 [17]. The secondary phases degrade cell performance due to their lower specific capacity and higher impedance. In addition to chemical reactions, mutual ion diffusion at the interfaces is another common phenomenon. Aluminum, a common dopant of LLZO, can diffuse into LCO to form doped/substituted LiAl_x-Co_{1-x}O₂ [49,50], and Co-ions from LCO can diffuse into LLZO to form various Co-containing reaction products such as LLZO:Co, LCO or Li_{0.5}La₂Co_{0.5}O_{4. [21]}. The ion diffusion can occur in the composite cathode as well as between the cathode and the separator [21]. Furthermore, high sintering temperatures can lead to partial delamination of the cathode from the separator [51] or to the formation of cracks in the ceramic particles of the cathode and separator, resulting in increased resistance, reduced mechanical stability of the cathode, and potentially isolated CAM material [52,53]. Crack formation is of particular concern in photonic sintering techniques, in which mainly the surface is heated at high rates, resulting in strong temperature gradients towards the substrate. In addition, high temperatures during sintering can lead to a loss of Li-ions from LLZO, resulting in the formation of an insulating La₂Zr₂O₇ pyrochlore phase [21,22]. Furthermore, the cubic LLZO phase may undergo a phase transition to the tetragonal phase or the low-temperature cubic phase, both of which have lower ionic conductivity [4,54]. The tetragonal phase may be formed by diffusion of substituents (which stabilize the cubic crystal phase) from LLZO into the CAM [21,49,50]. The low temperature cubic LLZO phase can form due to processing at lower temperatures in the presence of H₂O and the corresponding $Li^+ \leftrightarrow H^+$ exchange [54,55].

The main objective in sintering composite cathodes is to achieve a phase-pure, dense, well-connected layer without the above-mentioned phenomena in the separator and cathode. To ensure this, the material and the sintering process must be adjusted to reduce or avoid the negative effects (Fig. 1) as much as possible to guarantee good electrochemical properties. Further, the sintering process that can avoid the most negative effects and at the same time is the most economical is the most attractive for future industrial application.

To proof the suitability of the blacklight sintering with a multi-pulse

Xe flash lamp for sintering of LCO-LLZO ceramic composite cathodes, samples were produced after the schematic shown in Fig. 2a. The resulting half-cells after blacklight sintering were analyzed with respect to microstructure, crystallographic phase as well as electrochemical performance.

In order to perform the optimization of the sintering parameters two consecutive pulse programs were used for each sample at a frequency of 60 Hz and a constant voltage of 220 V. The first heating program varied in pulse length and total number of pulses, while the second program had a constant sequence with a pulse length of 0.4 ms and 600 pulses, Table 1.

For the first heating step, three different sintering modes were selected, differing in pulse length and number of pulses (Table 1). Optical images of the resulting representative half-cells are shown in Fig. 2b along with the half-cell before sintering. The sintering mode designated as "LT" (low temperature) resulted in a low achieved temperature and thus insufficient sintering. The sequence "MT" (medium temperature) resulted in medium temperatures and thus better sintering. The sequence "HT" (high temperature) led to overheating of the sample, so that the half-cell showed signs of thermal decomposition. The initial grey surface of the cathode layer became darker after sintering with the LT and MT sequence. The surface of the sample sintered with the HT sequence became almost black and the sample developed cracks after sintering, showing that the longer pulses lead to severe heating of the sample even with the smaller number of pulses and should be avoided.

Since the cathode material can react with the electrolyte at elevated temperatures, it is important to find process parameters where the phases are preserved [17–20]. Therefore, XRD and Raman spectroscopy measurements with a component analysis of individual phases were performed on the processed samples (Fig. 3a, b).

The Raman spectra of the samples with the separated LLZO phase are shown in Fig. 3a with a reference of untreated cubic LLZO. The signals of the samples can be assigned to the cubic LLZO phase, which include the vibrational modes of La cations at 109 cm⁻¹ (T_{2g}) and 122 cm⁻¹ (E_g); the broad signals of O bending at 215 cm⁻¹ (T_{2g}), and 251 cm⁻¹ (A_{1g}); the Li vibrational modes at 372 cm⁻¹ (T_{2g}), 417 cm⁻¹ (E_g or T_{2g}), 514 cm⁻¹ (E_g or T_{2g}); the signals of Zr-O bond stretching at 647 cm⁻¹ (A_{1g}); and the signal of the TaO₆ octahedron stretching at 741 cm⁻¹ from the Ta substitution [4,56-58]. Despite the Raman phase separation, some lowintensity residual signals may appear in the spectra; therefore, some LCO signals are also present in the LLZO spectra. In addition, the signals at 157 cm⁻¹ and 193 cm⁻¹ indicate the presence of Li₂CO₃ [55,59]. The interaction of LCO and LLZO at elevated temperatures can lead to a Co-ion diffusion into the LLZO, forming LLZO:Co [15,35]. This phase generates a photoluminescence at 693/694 cm⁻¹ [15,35], which is present in all samples. However, no evidence of other secondary phases can be found.

The separated spectra of the LCO phase with an LCO reference are shown in Fig. 3b. The rhombohedral LCO phase (space group $R\overline{3}m$)

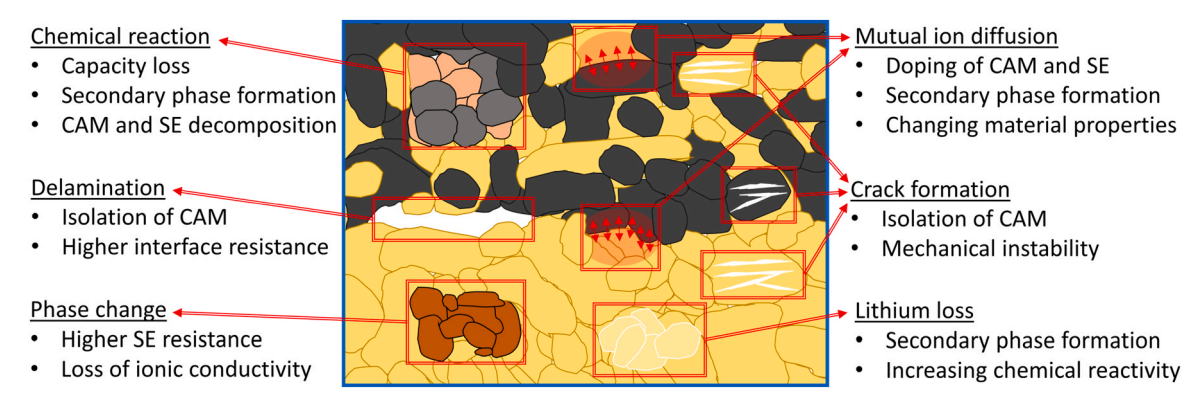


Fig. 1. Examples for different detrimental effects that can occur during the sintering of an LCO-LLZO composite cathode on a LLZO separator.

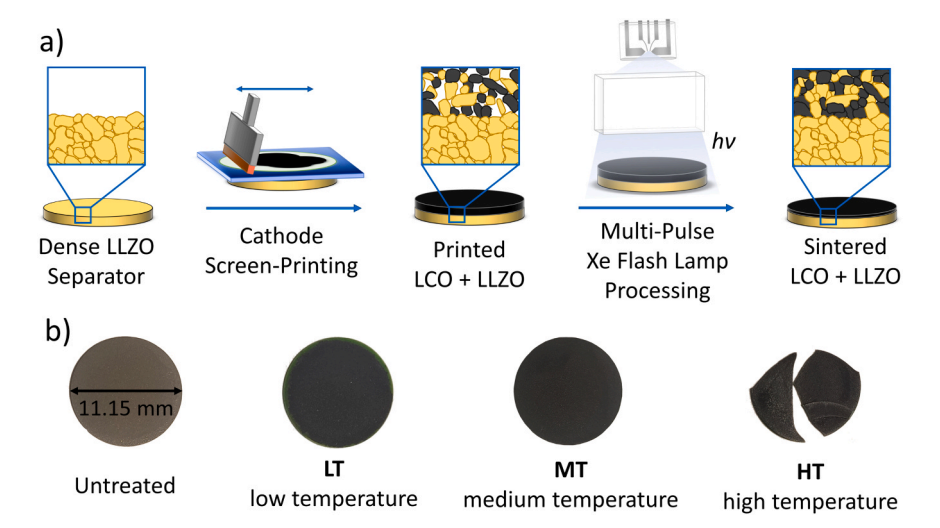


Fig. 2. a) schematic representation of sample preparation and processing with sections of the microstructure. First, only the dense LLZO is shown (LLZO = yellow grains), on which the porous green body of the composite cathode is screen-printed (LCO = dark grains), which is subsequently sintered and the density is increasing; b) images of the cathode surface in the untreated condition and after processing of 3 different pulse sequences. The processing parameters are shown in Table 1.

Table 1Pulse parameters of the pulse sequences LT, MT, HT with the number of pulses, pulse length, and sintering time. The pulse frequency was always at 60 Hz.

Sequence	1 st Heating		2 nd Heating		Total sintering
	Pulse length	No. of pulses	Pulse length	No. of pulses	time
LT	0.7 ms	1200	0.4 ms	600	30 s
MT	0.9 ms	600	0.4 ms	600	20 s
HT	1.0 ms	600	0.4 ms	600	20 s

with the Raman signals at 488 cm $^{-1}$ (E_g) and 597 cm $^{-1}$ (A_{1g}) is present in all samples [60,61]. However, a shift of 4 cm $^{-1}$ to lower wavenumbers is observed in all processed samples. This shift indicates a loss of Li from the LCO lattice during flash lamp processing [62], which is similar to Li losses during RTP sintering of pure LCO layers [36], but more pronounced compared to RTP sintering of LCO-LLZO composite cathode layers [35].

In addition to Raman spectroscopy, XRD measurements were performed. The XRD patterns of the composite cathodes (Fig. 3c) demonstrates that LLZO (ICSD 422259) and LCO (ICDD 010702685) phases are preserved in the cathodes sintered with LT and MT sequences, while the cathode sintered with HT sequence shows strongly decreased intensity of LCO phase, indicating its decomposition. In addition, minor reflections of Li₂CoZrO₄ (ICDD 000400367) are present, which is likely formed by a reaction of LCO and LLZO. Nevertheless, the LLZO signals are still present.

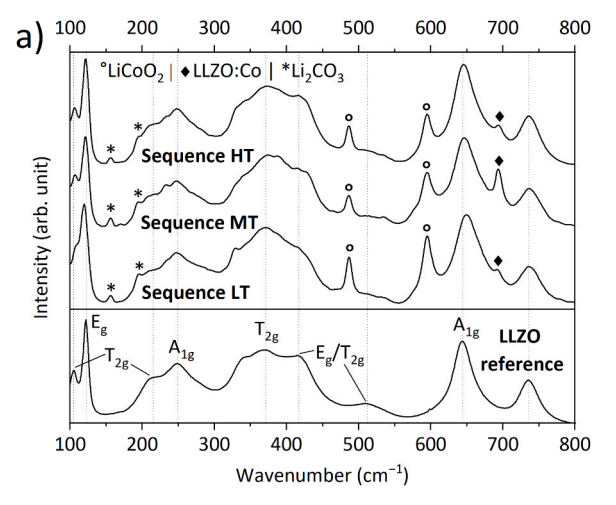
XRD and Raman phase analyses show that the parameters of the LT and MT sequence do not lead to decomposition of LCO and LLZO phases during sintering. However, minor loss of Li in LCO and the formation of LLZO:Co require further adjustment of the processing parameters to avoid these effects. The sequence HT with the longest pulse length of 1.0 ms leads to a reduced intensity of LCO in the XRD pattern and the formation of a secondary phase, which confirms the above observation of poor suitability of HT sequence for sintering due to too high temperature during annealing.

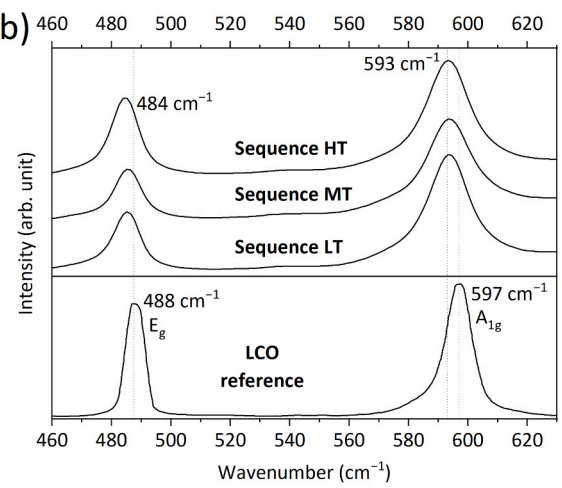
In addition to the chemical composition, the microstructure of the cathode layers is also important for cell performance. Scanning electron microscopy (SEM) images of the surface of composite cathodes are shown in Fig. 4. Compared to the surface of the cathode before sintering (Fig. 4a), it is clear that sintering with the LT sequence results in coarsening and rounding of the LCO particles (dark contrast) and LLZO particles (light contrast) (Fig. 4b), indicating possible surface diffusion

or evaporation and condensation during heat treatment. However, the connections between the particles are insufficient, indicating insufficient energy transfer and low temperature during sintering. The cathode formed by the MT sequence (Fig. 4c) consists of larger particles, which is due to increased diffusion and particle coarsening during processing. In some places, there are large gaps between the LCO and LLZO particles, but in other areas they are well connected. The microstructure of this sample clearly shows that a longer pulse length, even with a lower total number of pulses, results in higher temperatures and much better sintering behavior, although it makes the surface of the composite cathodes rougher. Some even darker areas on the surface (marked in the white box, Fig. 4c) probably belong to Li₂CO₃ [55] which has already been detected by Raman spectroscopy (Fig. 3a). This could be related to the observed Li loss from the LCO, where evaporated Li oxides are subsequently deposited on the cathode surface where they react with ambient atmosphere to form Li_2CO_3 , but it could also result from $Li^+ \leftrightarrow H^+$ exchange in LLZO when exposed to ambient air [55]. The cathode processed with the HT sequence (Fig. 4d), whose decomposition was detected in the XRD analysis, shows strong particle coarsening. However, the LCO particles have a different morphology than those in the cathode sintered with the MT sequence, especially at the particle edges, suggesting that other Co-containing phases observed in the XRD analysis, such Li₂CoZrO₄, may also be present. In addition, a larger area is covered with dark contrast material (marked in the white box, Fig. 4d), which probably belongs to Li₂CO₃, indicating a higher Li loss from the material.

To assess the sintering depth, the connection of cathode and separator, and the microstructure of the separator, cross-sections of the samples were examined by SEM (Fig. 5). The LT sequence (Fig. 5a, b) again shows insufficient sintering, in agreement with the top view SEM image in Fig. 4b. The cross-section image shows that the connectivity between the particles and between the separator and cathode layers is low, so there are probably not enough ionic and electronic paths. The separator itself does not show any changes after processing.

For the cathode sintered with the MT sequence (Fig. 5c, d), many interconnections between the LCO and LLZO particles can be seen, which were formed during sintering. Therefore, the required electronic and ionic pathways are present, and the cathode can be electrochemically cycled. However, many cracks parallel to the surface can be seen in the top layer of LLZO particles directly exposed to the blacklight radiation. These cracks act as a barrier for ionic conductivity and can effectively reduce the capacity of the cathode due to losing contact to CAM. The origin of these cracks is probably a thermal shock with strong





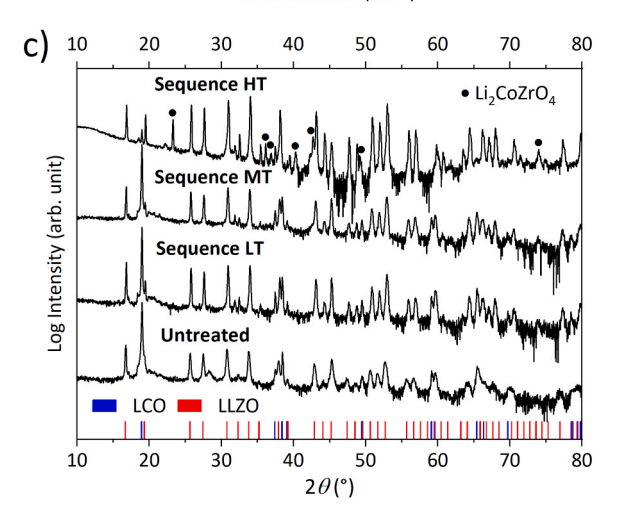


Fig. 3. Raman spectroscopy and XRD measurements of the composite cathodes treated with sequence LT, MT, and HT. The Raman spectra were separated by their phases (LLZO and LCO) to prevent superposition of the several signals: a) LLZO Raman spectra with LLZO reference spectra with marked vibrational modes [57]; b) LCO Raman spectra with LCO reference spectra with marked vibrational modes [60,61]; c) XRD patterns of the processed and untreated composite cathodes with the reference pattern of LLZO (red, ICSD 422259) and LCO (blue, ICDD 010702685). For better identification of the low concentrated secondary phases the XRD is shown in a logarithmic plot.

temperature gradients due to the short and intense heating and cooling conditions, which likely generate mechanical stresses. Looking at the entire cross-section, it is noticeable that the cracks can only be found in the uppermost micrometers, as this is where the thermal gradients are expected to be highest and should be significantly less pronounced in the areas below. Accordingly, further improvement of this processing method should focus on reducing the crack formation. A possible solution could be to tailor the heating and cooling schedule with dedicated ramps to and from high temperature, or/and to reduce the pulse length while increasing the number of pulses. In contrast, the LCO particles show no signs of cracking. This is probably related to the higher thermal conductivity of LCO with 5.4 W K⁻¹ m⁻¹ [63] compared to LLZO with 1.5 W K⁻¹ m⁻¹ [64]. This difference could result in less temperature gradient and less thermal stresses within the LCO, but also in a stronger temperature gradient in the LLZO particles close to the LCO as the heat flux is piled up there, possibly resulting in mechanical stresses and cracking. In addition, the size of LLZO particles in the cathode and separator sintered with the MT sequence increased to $10.9 \pm 0.7 \ \mu m$ compared to the LT sequence with 8.8 \pm 2.2 μm , indicating that during the MT sequence the temperature was high enough to further densify the already dense LLZO separator material.

In the cross-section of the cathode, processed with the HT sequence with the longest pulse length (Fig. 5e, f), the LCO phase was found inside the LLZO separator at a distance of more than 100 µm from the cathode separator interface, and the initial composite cathode layer has almost completely disappeared. For better illustration, the dark contrast of the LCO is shown in red in Fig. 6. As mentioned earlier, LCO can form at grain boundaries of LLZO separator after diffusion of Co-ions from the cathode [21]. However, LCO infiltration into the separator extends over more than 100 µm and forms micrometer-thick layers along the LLZO grain boundary network. Therefore, Co-ion diffusion is probably not the main mechanism. More likely, the LCO infiltration is related to the high temperature that can be reached by the Xe flash lamp (up to 2000 °C) [45] and thus to the melting of the LCO into a liquid with unknown composition. Capillarity could transport the melt into the pore channels of the LLZO, where it solidifies into the phases observed by XRD and Raman spectroscopy. The entire cross-section image shows a clear difference in microstructure in the first 100 µm below the cathode, compared to the rest of the separator. This is partly due to the new phase that has now accumulated in the pores, but it can also be assumed that during sintering cracking has again taken place. Due to the high temperatures in the HT sequence, it is possible that some of the cracks are sintered again in the further course of processing, but the porosity in this area remains slightly increased compared to the rest of the separator.

The diffusion of Co-ions from the cathode into the separator during sintering is another undesirable process that degrades the performance of the cell. Therefore, the degree of Co-ion diffusion can be used as an additional parameter to evaluate the sintering process [15,21,35]. Since the typical products of Co-ion diffusion, LCO and LLZO:Co, are highly Raman active (LCO, 597 cm⁻¹) or generates a strong photoluminescence while using a 532 nm laser (LLZO:Co, 693 cm⁻¹), it is possible to use Raman spectroscopy to evaluate the depth of contamination of the LLZO separator during cathode sintering. Raman measurement of the half-cell sintered in the MT sequence was recorded in a range of 30 µm over the whole half-cell in 1 µm steps (x and y) and the resulting signals were averaged line-wise parallel to the cathode and normalized to the highest signal intensity (Fig. 7). The LCO phase has the highest signal intensity in the cathode, which decreases dramatically at the cathode separator interface. In the separator, the LCO signals are still present up to a depth of $\sim 100 \ \mu m$. An even higher degree of contamination is observed in the distribution of the LLZO:Co phase, which is present in the first \sim 120 μm of the separator. Compared to RTP sintering of similar samples (1000 °C, 90 s), which show contamination depth of \sim 700 µm [35,36], much lower contamination occurred in the present study. The lower Co-ion diffusion into the separator in blacklight sintering is likely due to the shorter sintering times and stronger thermal gradients in the cathode

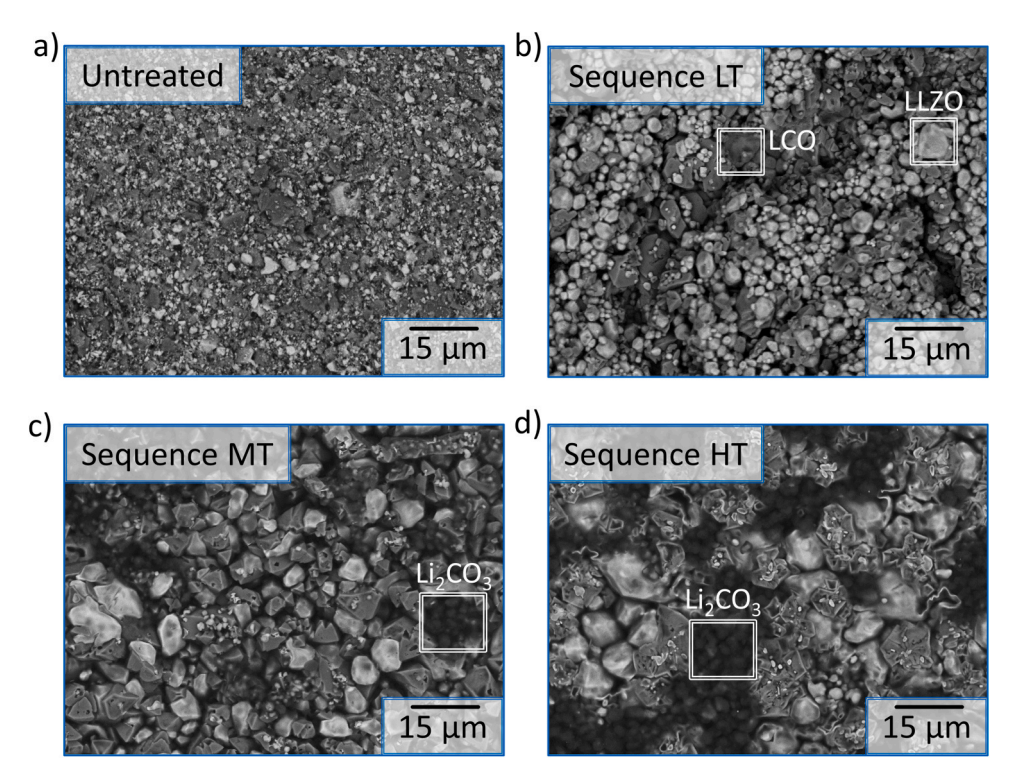


Fig. 4. Top-view SEM images (BSE) of the flash lamp processed composite cathodes: a) untreated; b) sequence LT including white labels LCO and LLZO; c) sequence MT with labeled Li_2CO_3 ; d) sequence HT with labeled Li_2CO_3 .

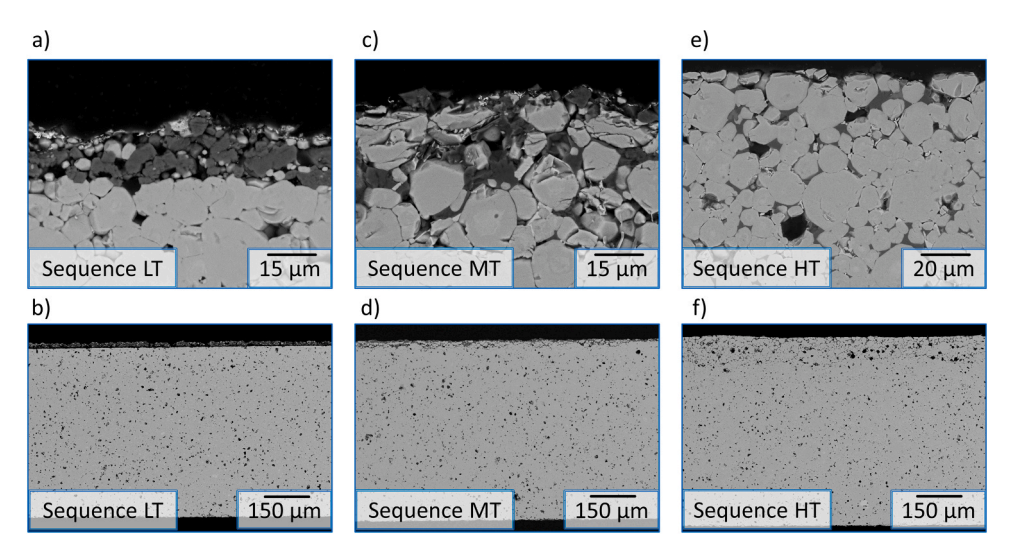
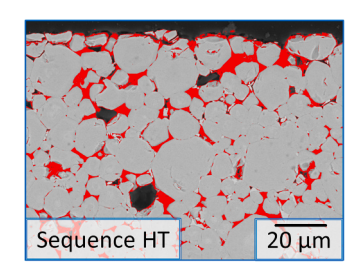


Fig. 5. Polished cross-sections of the flash lamp processed half-cells: a) and b) sequence LT; c) and d) sequence MT; e) and f) sequence HT.



 $\begin{tabular}{ll} Fig. 6. Cross-section of sequence HT (Fig. 5e) with highlighted LCO contrast in red. \\ \end{tabular}$

layer and the separator. By these thermal gradients, the high

temperatures which increases the Co-ion diffusion are reduced to a limited volume of the upper separator region close to the cathode [21]. In deeper separator regions the temperature is lower and the Co-ion diffusion is consequently lower or not present. This behavior makes the blacklight sintering of cathode layers attractive for the ceramic cell production, since it offers the possibility of sintering the cathode layer, while reducing detrimental interactions with the separator.

To investigate the electrochemical performance of the sintered half-cells, an In foil was attached as the anode on the other side of the LLZO separator and full cells were tested using galvanostatic cycling with potential limitation (GCPL). The samples sintered in the LT, and HT sequences showed almost no electrochemical activity. This behavior of the LT sample was probably due to an insufficient contact between the particles in the cathode, and in the case of the HT sample, due to the

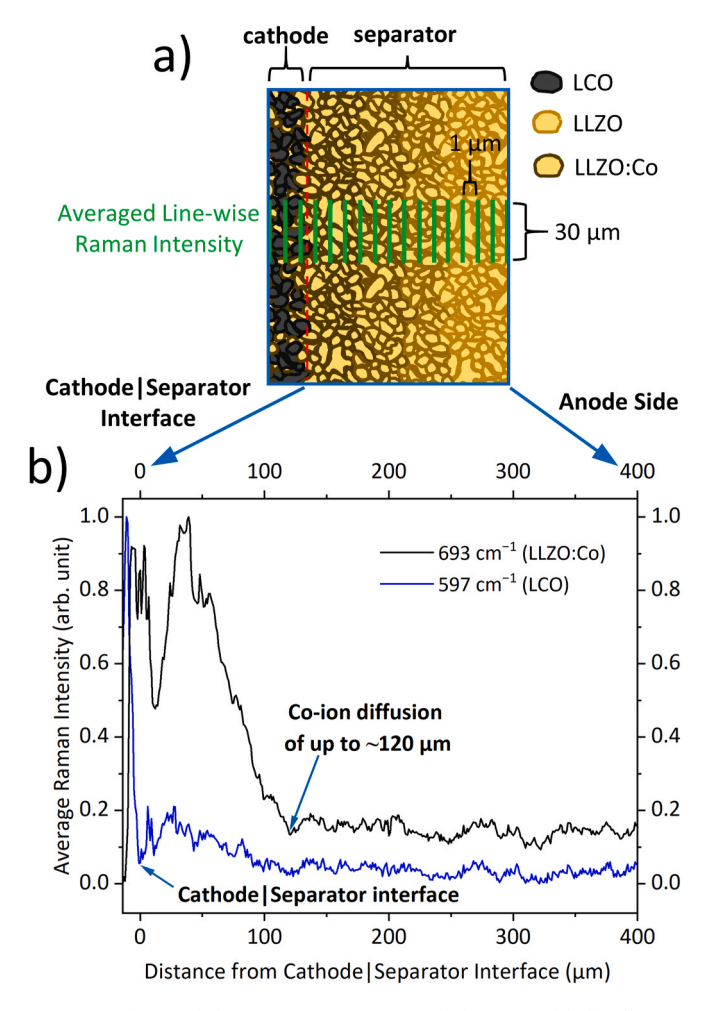


Fig. 7. a) scheme of the Raman measurement of the sintered half-cell cross-section processed with sequence MT to detect Co-ion diffusion into the LLZO separator as a function of distance from the cathode|separator interface. The measurement was performed in a range of 30 μm over the whole half-cell in 1 μm steps (x and y) and the resulting signals were averaged line-wise and normalized; b) Raman spectra with the LLZO:Co photoluminescence signal at 693 cm $^{-1}$ (black) and the LCO phase signal at 597 cm $^{-1}$ (blue) are shown as a function of distance from the cathode|separator interface (0 μm).

severe material degradation discussed above. In contrast, the sample sintered with the MT sequence (the only sample with sufficient sintering and only low amounts of secondary phases) could be charged and discharged over 10 cycles (Fig. 8a). A very high initial capacity of 313 mAh g⁻¹ was obtained in the first charge cycle (inset in Fig. 8a), but this process was largely irreversible, and only 19% of the capacity could be reversibly extracted in the subsequent discharge. The coulombic efficiency (CE) (Fig. 8b) increased from 19% in the first cycle to 72% in the 10th cycle, but remained generally lower than values obtained for comparable LCO-LLZO cells fabricated by other sintering techniques [14,15,35,65]. The reasons for the large irreversible losses during the first charge are still unknown and would require further investigation. Conceivable causes would be the formation of the Li-In alloy on the anode side [66], irreversible phase transformation of LCO and LLZO during cycling [67], and/or electrochemical decomposition of Li₂CO₃ impurities [68].

The first discharge had a specific capacity of $\sim\!60$ mAh g⁻¹, corresponding to a CAM utilization of 43% (with 140 mAh g⁻¹ as the practical capacity of LCO [69]). The cracks in the LLZO particles observed in the cross-section SEM image (Fig. 5c, d) are the most obvious reason for the moderate CAM utilization, as they impede the charge transport pathways through the electrode and increase the electrode resistance. The

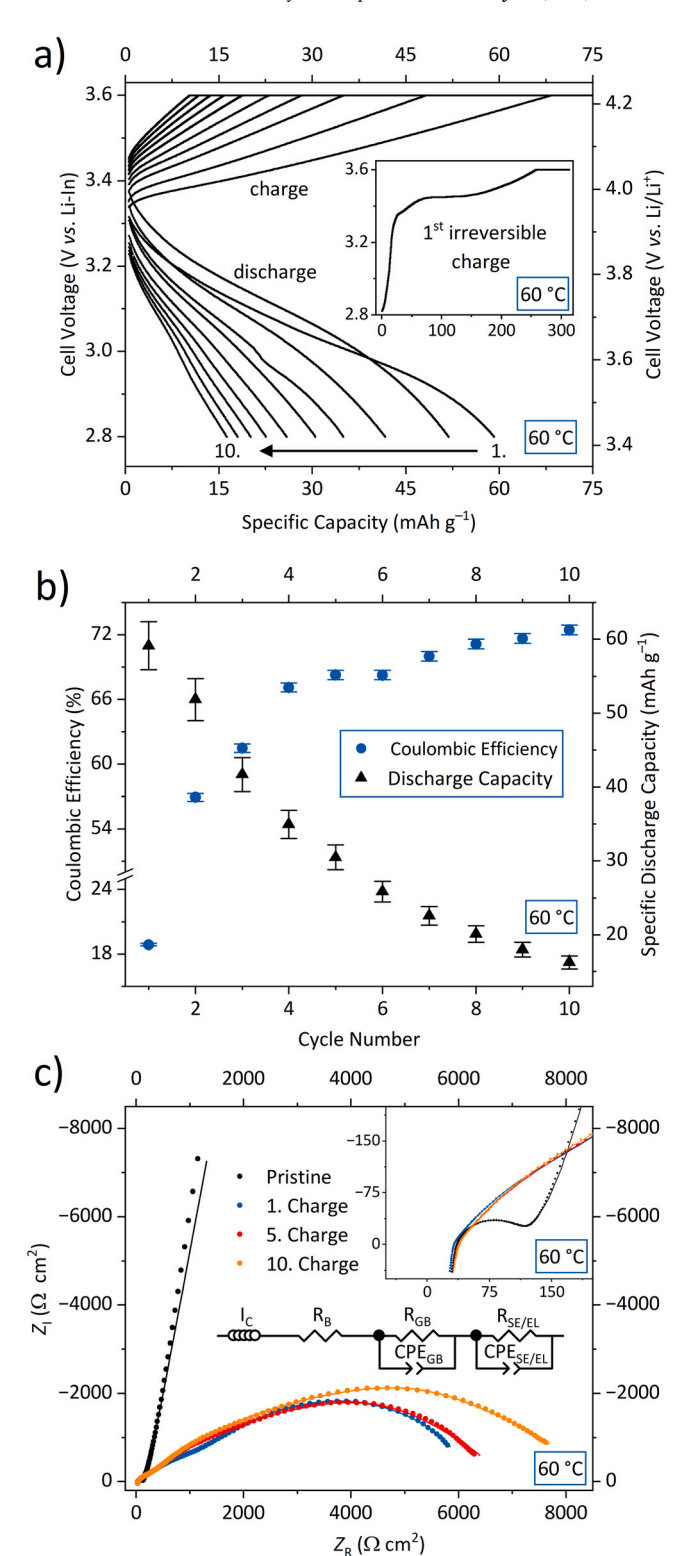


Fig. 8. Electrochemical analysis of the cell composed of the cathode half-cell processed with the MT sequence and a Li-In anode: a) GCPL measurements, with the first charge shown in the inset. The potentials against Li-In and against Li/Li⁺ are shown for better comparability [75,76]; b) the corresponding coulombic efficiency and discharge capacity of each electrochemical cycle; c) the Nyquist plot of the EIS measurements before and during GCPL. The spectra were fitted with the equivalent circuit shown in the inset, where I_c represents the inductive effect of the cables, R_B represents the resistance of the LLZO bulk, the R-CPE $_{\rm SE/EL}$ element represents the LLZO grain boundary resistance, and the R-CPE $_{\rm SE/EL}$ element represents the electrolyte electrode interface resistance (R-CPE $_{\rm SE/EL}$ = R-CPE $_{\rm SE/Cathode}$ + R-CPE $_{\rm SE/Anode}$).

capacity decreases with each subsequent charge/discharge cycle, finally reducing the discharge capacity to $\sim \! 16$ mAh g $^{-1}$, corresponding to a CAM utilization of 11% after 10 cycles.

In addition to the capacity fading, an increase in cell resistance is observed in the electrochemical impedance spectroscopy (EIS) measurements (Fig. 8c). The pristine cell before electrochemical cycling shows a relatively low total impedance, which could not be deconvoluted with sufficient accuracy due to a strong overlap of different electrode contributions, including the In anode [70,71]. Already after the first charge, the cell impedance increased significantly. A stretched semicircle probably corresponding to the separator electrode interfaces $(R_{SE/EL} = R_{SE/cathode} + R_{SE/anode})$ was observed In the Nyquist plot with a resistance of 6231 $\Omega\,\text{cm}^2$ and a capacitance of $\sim\!10^{-5}\,\text{F},$ obtained after fitting with the equivalent circuit shown in Fig. 8c [65,72,73]. This resistance increased to a value of 8461 Ω cm² by the 10th charge. Capacity fading during cycling, accompanied by an increase in cell impedance, is common in all-solid-state garnet-based cells, which is mainly due to the electrochemical instability of the unprotected LCO LLZO interface and the mechanical degradation of the composite cathode during cycling [14,15,50,65,74]. Compared to similar garnet-based SSBs fabricated by other techniques, the blacklight sintered cells still exhibit lower initial capacity and faster capacity degradation, which is probably due to the cracking of LLZO particles as described above. Further process optimization should therefore focus on thermal relaxation in the system during sintering to prevent cracking, which could hypothetically be achieved by a lower pulse frequency or additional pulse programs for heating and cooling.

4. Conclusion

Blacklight sintering was demonstrated to be a promising option for time- and energy-efficient processing of LLZO-based composite cathodes for solid-state-batteries. Taking advantage of the temperature dependent high absorption of near-UV light, sintering of a LCO-LLZO composite cathode on a LLZO separator produced a functioning cell in only 20 s. Unlike other photonic sintering techniques, such as rapid thermal processing (RTP), blacklight sintering reduced the unwanted diffusion of Co-ions from the composite cathode into the LLZO separator. Using an In anode for electrochemical cycling tests, a specific capacity of ~60 mAh g⁻¹ was achieved during the first discharge. The rather low cathode utilization of 43% was attributed to cracking in the LLZO particles along the cathode surface, probably caused by a thermal shock in the sintering process. These results point to clear directions for optimization of this promising processing route, which should focus on thermal relaxation in the system during sintering to prevent cracking. With proper optimization of the blacklight sintering process, it can provide an industrially attractive route for processing oxide ceramic components for solid-state batteries.

CRediT authorship contribution statement

Walter Sebastian Scheld: Data curation, Methodology, Investigation, Validation, Visualization, Writing – original draft. Julian N. Ebert: Methodology, Writing – review & editing. Michael Scherer: Conceptualization, Methodology. Lovro Fulanovic: Conceptualization. Lukas Porz: Conceptualization. Christian Dellen: Validation, Writing – review & editing. Martin Ihrig: Conceptualization, Writing – review & editing. Sven Uhlenbruck: Funding acquisition, Writing – review & editing. Martin Finsterbusch: Conceptualization, Funding acquisition, Writing – review & editing. Olivier Guillon: Conceptualization, Funding acquisition, Writing – review & editing. Dina Fattakhova-Rohlfing: Conceptualization, Funding acquisition, Writing – review & editing. Wolfgang Rheinheimer: Conceptualization, Methodology, Funding acquisition, Writing – review & editing.

Declaration of Competing Interest

The authors declare that they have no known competing financial interests or personal relationships that could have appeared to influence the work reported in this paper.

Acknowledgment

This work was funded by the German Federal Ministry for Economic Affairs and Climate Action (BMWK) within the OptiKeraLyt project (grant no. 03ETE016F), as well as by the German Federal Ministry of Education and Research (BMBF) as part of the FestBatt2-Oxide (grant no. 13XP0434A) and CatSE^2 (grant no. 13XP0510A) projects. Wolfgang Rheinheimer acknowledges the funding by the DFG (Emmy-Noether-Programme, RH146/1–1).

References

- J. Janek, W.G. Zeier, A solid future for battery development, Nat. Energy 1 (9) (2016)
- [2] T. Thompson, S. Yu, L. Williams, R.D. Schmidt, R. Garcia-Mendez, J. Wolfenstine, J.L. Allen, E. Kioupakis, D.J. Siegel, J. Sakamoto, Electrochemical Window of the Li-Ion Solid Electrolyte Li₇La₃Zr₂O₁₂, ACS Energy Lett. 2 (2) (2017) 462–468.
- [3] R. Murugan, V. Thangadurai, W. Weppner, Fast lithium ion conduction in garnettype Li₇La₃Zr₂O₁₂, Angew. Chem. Int. Ed. 46 (41) (2007) 7778–7781.
- [4] T. Thompson, J. Wolfenstine, J.L. Allen, M. Johannes, A. Huq, I.N. David, J. Sakamoto, Tetragonal vs. cubic phase stability in Al – free Ta doped Li₇La₃Zr₂O₁₂ (LLZO), J. Mater. Chem. A 2 (33) (2014) 13431–13436.
- [5] C.-L. Tsai, E. Dashjav, E.-M. Hammer, M. Finsterbusch, F. Tietz, S. Uhlenbruck, H. P. Buchkremer, High conductivity of mixed phase Al-substituted Li₇La₃Zr₂O₁₂, J. Electroceram. 35 (14) (2015) 25–32.
- [6] M. Mann, M. Kupers, G. Hauschen, M. Finsterbusch, D. Fattakhova-Rohlfing, O. Guillon, Evaluation of Scalable Synthesis Methods for Aluminum-Substituted Li₇La₃Zr₂O₁₂ Solid Electrolytes, Materials 14 (22) (2021).
- [7] M. Mann, M. Küpers, G. Häuschen, M. Finsterbusch, D. Fattakhova-Rohlfing, O. Guillon, The influence of hafnium impurities on the electrochemical performance of tantalum substituted Li₇La₃Zr₂O₁₂ solid electrolytes, Ionics 28 (1) (2021) 53–62.
- [8] M. Ihrig, T.P. Mishra, W.S. Scheld, G. Hauschen, W. Rheinheimer, M. Bram, M. Finsterbusch, O. Guillon, Li₇La₃Zr₂O₁₂ solid electrolyte sintered by the ultrafast high-temperature method, J. Eur. Ceram. Soc. 41 (12) (2021) 6075–6079.
- [9] C. Wang, K. Fu, S.P. Kammampata, D.W. McOwen, A.J. Samson, L. Zhang, G. T. Hitz, A.M. Nolan, E.D. Wachsman, Y. Mo, V. Thangadurai, L. Hu, Garnet-Type Solid-State Electrolytes: Materials, Interfaces, and Batteries, Chem. Rev. 120 (10) (2020) 4257–4300.
- [10] R. Ye, N. Hamzelui, M. Ihrig, M. Finsterbusch, E. Figgemeier, Water-Based Fabrication of a Li|Li₇La₃Zr₂O₁₂|LiFePO₄ Solid-State Battery—Toward Green Battery Production, ACS Sustain. Chem. Eng. 10 (23) (2022) 7613–7624.
- [11] M. Finsterbusch, T. Danner, C.L. Tsai, S. Uhlenbruck, A. Latz, O. Guillon, High Capacity Garnet-Based All-Solid-State Lithium Batteries: Fabrication and 3D-Microstructure Resolved Modeling, ACS Appl. Mater. Interfaces 10 (26) (2018) 22329–22339.
- [12] K.J. Kim, J.L.M. Rupp, All ceramic cathode composite design and manufacturing towards low interfacial resistance for garnet-based solid-state lithium batteries, Energy Environ. Sci. 13 (12) (2020) 4930–4945.
- [13] M. Rosen, M. Finsterbusch, O. Guillon, D. Fattakhova-Rohlfing, Free standing dual phase cathode tapes – scalable fabrication and microstructure optimization of garnet-based ceramic cathodes, J. Mater. Chem. A 10 (5) (2022) 2320–2326.
- [14] M. Ihrig, M. Finsterbusch, C.-L. Tsai, A.M. Laptev, C.-h Tu, M. Bram, Y.J. Sohn, R. Ye, S. Sevinc, S.-k Lin, D. Fattakhova-Rohlfing, O. Guillon, Low temperature sintering of fully inorganic all-solid-state batteries Impact of interfaces on full cell performance, J. Power Sources 482 (2021), 228905.
- [15] C.-L. Tsai, Q. Ma, C. Dellen, S. Lobe, F. Vondahlen, A. Windmüller, D. Grüner, H. Zheng, S. Uhlenbruck, M. Finsterbusch, F. Tietz, D. Fattakhova-Rohlfing, H. P. Buchkremer, O. Guillon, A garnet structure-based all-solid-state Li battery without interface modification: resolving incompatibility issues on positive electrodes, Sustain, Energy Fuels 3 (1) (2019) 280–291.
- [16] S. Uhlenbruck, J. Dornseiffer, S. Lobe, C. Dellen, C.-L. Tsai, B. Gotzen, D. Sebold, M. Finsterbusch, O. Guillon, Cathode-electrolyte material interactions during manufacturing of inorganic solid-state lithium batteries, J. Electroceram. 38 (24) (2016) 197–206.
- [17] J. Wakasugi, H. Munakata, K. Kanamura, Thermal Stability of Various Cathode Materials against Li_{6.25}Al_{0.25}La₃Zr₂O₁₂ Electrolyte, J. Electrochem. Soc. Jpn. 85 (2) (2017) 77–81.
- [18] N. Zhang, X. Long, Z. Wang, P. Yu, F. Han, J. Fu, G. Ren, Y. Wu, S. Zheng, W. Huang, C. Wang, H. Li, X. Liu, Mechanism Study on the Interfacial Stability of a Lithium Garnet-Type Oxide Electrolyte against Cathode Materials, ACS Appl. Energy Mater. 1 (11) (2018) 5968–5976.
- [19] Y. Ren, T. Liu, Y. Shen, Y. Lin, C.-W. Nan, Chemical compatibility between garnet-like solid state electrolyte Li_{6.75}La₃Zr_{1.75}Ta_{0.25}O₁₂ and major commercial lithium battery cathode materials, J. Mater. 2 (3) (2016) 256–264.

- [20] L. Miara, A. Windmuller, C.L. Tsai, W.D. Richards, Q. Ma, S. Uhlenbruck, O. Guillon, G. Ceder, About the Compatibility between High Voltage Spinel Cathode Materials and Solid Oxide Electrolytes as a Function of Temperature, ACS Appl. Mater. Interfaces 8 (40) (2016) 26842–26850.
- [21] W.S. Scheld, K. Kim, C. Schwab, A.C. Moy, S.K. Jiang, M. Mann, C. Dellen, Y. J. Sohn, S. Lobe, M. Ihrig, M.G. Danner, C.Y. Chang, S. Uhlenbruck, E. D. Wachsman, B.J. Hwang, J. Sakamoto, L.F. Wan, B.C. Wood, M. Finsterbusch, D. Fattakhova-Rohlfing, The Riddle of Dark LLZO: Cobalt Diffusion in Garnet Separators of Solid-State Lithium Batteries, Adv. Funct. Mater. 33 (43) (2023) 2302939
- [22] A.M. Nolan, E.D. Wachsman, Y. Mo, Computation-guided discovery of coating materials to stabilize the interface between lithium garnet solid electrolyte and high-energy cathodes for all-solid-state lithium batteries, Energy Stor. Mater. 41 (2021) 571–580.
- [23] R.K. Bordia, S.J.L. Kang, E.A. Olevsky, Current understanding and future research directions at the onset of the next century of sintering science and technology, J. Am. Ceram. Soc. 100 (6) (2017) 2314–2352.
- [24] R.M. German. Sintering: from Empirical Observations to Scientific Principles, 1st ed., Butterworth-Heinemann, 2014.
- [25] E.F.S. Ciacco, J.R. Rocha, A.R. Coutinho, The energy consumption in the ceramic tile industry in Brazil, Appl. Therm. Eng. 113 (2017) 1283–1289.
- [26] A. Mezquita, J. Boix, E. Monfort, G. Mallol, Energy saving in ceramic tile kilns: Cooling gas heat recovery, Appl. Therm. Eng. 65 (1–2) (2014) 102–110.
- [27] M.N. Rahaman. Ceramic Processing and Sintering, 2nd ed., CRC Press, Boca Raton,
- [28] E. Worrell, L. Price, N. Martin, C. Hendriks, L.O. Meida, Carbon Dioxide Emissions from the Global Cement Industry, Annu. Rev. Environ. Resour. 26 (1) (2001) 303–329
- [29] H. Jouhara, N. Khordehgah, S. Almahmoud, B. Delpech, A. Chauhan, S.A. Tassou, Waste heat recovery technologies and applications, Therm. Sci. Eng. Prog. 6 (2018) 268–289.
- [30] T. Ibn-Mohammed, C.A. Randall, K.B. Mustapha, J. Guo, J. Walker, S. Berbano, S.C. L. Koh, D. Wang, D.C. Sinclair, I.M. Reaney, Decarbonising ceramic manufacturing: A techno-economic analysis of energy efficient sintering technologies in the functional materials sector, J. Eur. Ceram. Soc. 39 (16) (2019) 5213–5235.
- [31] B. Delpech, M. Milani, L. Montorsi, D. Boscardin, A. Chauhan, S. Almahmoud, B. Axcell, H. Jouhara, Energy efficiency enhancement and waste heat recovery in industrial processes by means of the heat pipe technology: Case of the ceramic industry, Energy 158 (2018) 656–665.
- [32] M. Castro Oliveira, M. Iten, P.L. Cruz, H. Monteiro, Review on energy efficiency progresses, technologies and strategies in the ceramic sector focusing on waste heat recovery, Energies 13 (22) (2020) 6096.
- [33] A.-N. Chen, J.-M. Wu, K. Liu, J.-Y. Chen, H. Xiao, P. Chen, C.-H. Li, Y.-S. Shi, High-performance ceramic parts with complex shape prepared by selective laser sintering: a review, Adv. Appl. Ceram. 117 (2) (2017) 100–117.
- [34] E. Gilshtein, S. Pfeiffer, M.D. Rossell, J. Sastre, L. Gorjan, R. Erni, A.N. Tiwari, T. Graule, Y.E. Romanyuk, Millisecond photonic sintering of iron oxide doped alumina ceramic coatings, Sci. Rep. 11 (1) (2021) 3536.
- [35] W.S. Scheld, S. Lobe, C. Dellen, M. Ihrig, G. Hauschen, L.C. Hoff, M. Finsterbusch, S. Uhlenbruck, O. Guillon, D. Fattakhova-Rohlfing, Rapid thermal processing of garnet-based composite cathodes, J. Power Sources 545 (2022), 231872.
- [36] W.S. Scheld, S. Lobe, S. Uhlenbruck, C. Dellen, Y.J. Sohn, L.C. Hoff, F. Vondahlen, O. Guillon, D. Fattakhova-Rohlfing, Rapid thermal sintering of screen-printed LiCoO₂ films, Thin Solid Films 749 (2022), 139177.
- [37] C.-a Lin, M. Ihrig, K.-c Kung, H.-c Chen, W.S. Scheld, R. Ye, M. Finsterbusch, O. Guillon, S.-k Lin, Low-temperature sintering of Li_{0.33}La_{0.55}TiO₃ electrolyte for all-solid-state Li batteries, J. Eur. Ceram. Soc. 43 (16) (2023) 7543–7552.
- [38] W.S. Scheld, L.C. Hoff, C. Vedder, J. Stollenwerk, D. Grüner, M. Rosen, S. Lobe, M. Ihrig, A.R. Seok, M. Finsterbusch, S. Uhlenbruck, O. Guillon, D. Fattakhova–Rohlfing, Enabling metal substrates for garnet-based composite cathodes by laser sintering, Appl. Energy 345 (2023).
- [39] L.C. Hoff, W.S. Scheld, C. Vedder, J. Stollenwerk, Laser sintering of ceramic-based solid-state battery materials, Laser-based Micro- and Nanoprocessing XVI Proceedings 11989 (2022).
- [40] M. Ihrig, R. Ye, A.M. Laptev, D. Grüner, R. Guerdelli, W.S. Scheld, M. Finsterbusch, H.-D. Wiemhöfer, D. Fattakhova-Rohlfing, O. Guillon, Polymer–Ceramic Composite Cathode with Enhanced Storage Capacity Manufactured by Field-Assisted Sintering and Infiltration, ACS Appl. Energy Mater. 4 (10) (2021) 10428–10432.
- [41] W. Ping, C. Wang, R. Wang, Q. Dong, Z. Lin, A.H. Brozena, J. Dai, J. Luo, L. Hu, Printable, high-performance solid-state electrolyte films, Sci. Adv. 6 (47) (2020) eabc8641.
- [42] L. Porz, M. Scherer, D. Huhn, L.M. Heine, S. Britten, L. Rebohle, M. Neubert, M. Brown, P. Lascelles, R. Kitson, D. Rettenwander, L. Fulanovic, E. Bruder, P. Breckner, D. Isaia, T. Frömling, J. Rödel, W. Rheinheimer, Blacklight sintering of ceramics, Mater. Horiz. 9 (6) (2022) 1717–1726.
- [43] M. Scherer, M.-G. Ameres, W. Rheinheimer, T. Frömling, J. Rödel, L. Fulanović, Blacklight sintering of BaTiO₃ ceramics, J. Eur. Ceram. Soc. 43 (12) (2023) 5406–5411.
- [44] L. Porz, M. Scherer, Q.K. Muhammad, K. Higuchi, Y. Li, S. Koga, A. Nakamura, W. Rheinheimer, T. Frömling, Microstructure and conductivity of blacklight-sintered TiO₂, YSZ, and Li_{0.33}La_{0.57}TiO₃, J. Am. Ceram. Soc. 105 (12) (2022) 7030–7035.
- [45] L. Rebohle, S. Prucnal, W. Skorupa, A review of thermal processing in the subsecond range: semiconductors and beyond, Semicond. Sci. Technol. 31 (10) (2016), 103001.

- [46] A. Bauer, C. Roitzheim, S. Lobe, Y.J. Sohn, D. Sebold, W.S. Scheld, M. Finsterbusch, O. Guillon, D. Fattakhova-Rohlfing, S. Uhlenbruck, Impact of Ni–Mn–Co–Al-Based Cathode Material Composition on the Sintering with Garnet Solid Electrolytes for All-Solid-State Batteries, Chem. Mater. 35 (21) (2023) 8958–8968.
- [47] K.H. Kim, Y. Iriyama, K. Yamamoto, S. Kumazaki, T. Asaka, K. Tanabe, C.A. J. Fisher, T. Hirayama, R. Murugan, Z. Ogumi, Characterization of the interface between LiCoO₂ and Li₇La₃Zr₂O₁₂ in an all-solid-state rechargeable lithium battery, J. Power Sources 196 (2) (2011) 764–767.
- [48] D.H. Jung, N. Umirov, T. Kim, Z. Bakenov, J.S. Kim, S.S. Kim, Thermal and structural stabilities of Li_xCoO₂ cathode for Li secondary battery studied by a temperature programmed reduction, Eurasia Chem. -Technol. J. 21 (1) (2019) 3–12.
- [49] N. Amdouni, H. Zarrouk, F. Soulette, C. Julien, LiAlyCo_{1-y}O₂ ($0.0 \le y \le 0.3$) intercalation compounds synthesized from the citrate precursors, Mater. Chem. Phys. 80 (1) (2003) 205–214.
- [50] K. Park, B.-C. Yu, J.-W. Jung, Y. Li, W. Zhou, H. Gao, S. Son, J.B. Goodenough, Electrochemical Nature of the Cathode Interface for a Solid-State Lithium-Ion Battery: Interface between LiCoO₂ and Garnet-Li₇La₃Zr₂O₁₂, Chem. Mater. 28 (21) (2016) 8051–8059.
- [51] P. Barai, T. Rojas, B. Narayanan, A.T. Ngo, L.A. Curtiss, V. Srinivasan, Investigation of Delamination-Induced Performance Decay at the Cathode/LLZO Interface, Chem. Mater. 33 (14) (2021) 5527–5541.
- [52] R. Koerver, W. Zhang, L. de Biasi, S. Schweidler, A.O. Kondrakov, S. Kolling, T. Brezesinski, P. Hartmann, W.G. Zeier, J. Janek, Chemo-mechanical expansion of lithium electrode materials – on the route to mechanically optimized all-solid-state batteries, Energy Environ. Sci. 11 (8) (2018) 2142–2158.
- [53] T. Liu, Y. Zhang, R. Chen, S.-X. Zhao, Y. Lin, C.-W. Nan, Y. Shen, Non-successive degradation in bulk-type all-solid-state lithium battery with rigid interfacial contact, Electrochem. Commun. 79 (2017) 1–4.
- [54] L. Dhivya, K. Karthik, S. Ramakumar, R. Murugan, Facile synthesis of high lithium ion conductive cubic phase lithium garnets for electrochemical energy storage devices, RSC Adv. 5 (116) (2015) 96042–96051.
- [55] R. Ye, M. Ihrig, N. Imanishi, M. Finsterbusch, E. Figgemeier, A Review on Li⁺/H⁺ Exchange in Garnet Solid Electrolytes: From Instability against Humidity to Sustainable Processing in Water, ChemSusChem 14 (20) (2021) 4397–4407.
- [56] G. Larraz, A. Orera, M.L. Sanjuán, Cubic phases of garnet-type $Li_7La_3Zr_2O_{12}$: the role of hydration, J. Mater. Chem. A 1 (37) (2013) 11419.
- [57] F. Tietz, T. Wegener, M.T. Gerhards, M. Giarola, G. Mariotto, Synthesis and Raman micro-spectroscopy investigation of Li₇La₃Zr₂O₁₂, Solid State Ion. 230 (2013) 77–82.
- [58] S. Uhlenbruck, C. Dellen, S. Möller, S. Lobe, C.-L. Tsai, M. Finsterbusch, M. Bram, O. Guillon, Reactions of garnet-based solid-state lithium electrolytes with water — A depth-resolved study, Solid State Ion. 320 (2018) 259–265.
- [59] D. Peltzer, J. Múnera, L. Cornaglia, Operando Raman spectroscopic studies of lithium zirconates during CO₂ capture at high temperature, RSC Adv. 6 (10) (2016) 8222–8231.
- [60] B.G.A. Freitas, J.M. Siqueira, L.M. da Costa, G.B. Ferreira, J.A.L.C. Resende, Synthesis and Characterization of LiCoO₂ from Different Precursors by Sol-Gel Method, J. Braz. Chem. Soc. 28 (11) (2017) 2254–2266.
- [61] T. Gross, C. Hess, Raman diagnostics of LiCoO₂ electrodes for lithium-ion batteries, J. Power Sources 256 (2014) 220–225.
- [62] T. Nishi, H. Nakai, A. Kita, Visualization of the State-of-Charge Distribution in a LiCoO₂ Cathode by In Situ Raman Imaging, J. Electrochem. Soc. 160 (10) (2013) A1785–A1788.
- [63] J. Cho, M.D. Losego, H.G. Zhang, H. Kim, J. Zuo, I. Petrov, D.G. Cahill, P.V. Braun, Electrochemically tunable thermal conductivity of lithium cobalt oxide, Nat. Commun. 5 (2014) 4035.
- [64] J. Neises, W.S. Scheld, A.-R. Seok, S. Lobe, M. Finsterbusch, S. Uhlenbruck, R. Schmechel, N. Benson, Study of thermal material properties for Ta- and Alsubstituted Li₇La₃Zr₂O₁₂ (LLZO) solid-state electrolyte in dependency of temperature and grain size, J. Mater. Chem. A 10 (22) (2022) 12177–12186.
- [65] M. Ihrig, M. Finsterbusch, A.M. Laptev, C.H. Tu, N.T.T. Tran, C.A. Lin, L.Y. Kuo, R. Ye, Y.J. Sohn, P. Kaghazchi, S.K. Lin, D. Fattakhova-Rohlfing, O. Guillon, Study of LiCoO₂/Li₇La₃Zr₂O₁₂:Ta Interface Degradation in All-Solid-State Lithium Batteries, ACS Appl. Mater. Interfaces 14 (9) (2022) 11288–11299.
- [66] Z. Wang, J. Zhao, X. Zhang, Z. Rong, Y. Tang, X. Liu, L. Zhu, L. Zhang, J. Huang, Tailoring lithium concentration in alloy anodes for long cycling and high areal capacity in sulfide-based all solid-state batteries, eScience 3 (1) (2023).
- [67] T. Okumura, T. Nakatsutsumi, T. Ina, Y. Orikasa, H. Arai, T. Fukutsuka, Y. Iriyama, T. Uruga, H. Tanida, Y. Uchimoto, Z. Ogumi, Depth-resolved X-ray absorption spectroscopic study on nanoscale observation of the electrode-solid electrolyte interface for all solid state lithium ion batteries, J. Mater. Chem. 21 (27) (2011).
- [68] A.A. Delluva, J. Kulberg-Savercool, A. Holewinski, Decomposition of Trace Li₂CO₃ During Charging Leads to Cathode Interface Degradation with the Solid Electrolyte LLZO, Adv. Funct. Mater. 31 (34) (2021) 2103716.
- [69] K. Mizushima, P.C. Jones, P.J. Wiseman, J.B. Goodenough, Li_xCoO₂ (0 < x < -1): A new cathode material for batteries of high energy density, Mater. Res. Bull. 15 (6) (1980) 783–789.
- [70] C. Sedlmeier, R. Schuster, C. Schramm, H.A. Gasteiger, A. Micro-Reference, Electrode for Electrode-Resolved Impedance and Potential Measurements in All-Solid-State Battery Pouch Cells and Its Application to the Study of Indium-Lithium Anodes, J. Electrochem. Soc. 170 (3) (2023).
- [71] W. Choi, H.-C. Shin, J.M. Kim, J.-Y. Choi, W.-S. Yoon, Modeling and Applications of Electrochemical Impedance Spectroscopy (EIS) for Lithium-ion Batteries, J. Electrochem. Sci. Technol. 11 (1) (2020) 1–13.

- [72] A.J. Samson, K. Hofstetter, S. Bag, V. Thangadurai, A bird's-eye view of Li-stuffed garnet-type Li₇La₃Zr₂O₁₂ ceramic electrolytes for advanced all-solid-state Li batteries, Energy Environ. Sci. 12 (10) (2019) 2957–2975.
- [73] J.T.S. Irvine, D.C. Sinclair, A.R. West, Electroceramics: Characterization by Impedance Spectroscopy, Adv. Mater. 2 (3) (1990) 132–138.
- [74] J. Sastre, X. Chen, A. Aribia, A.N. Tiwari, Y.E. Romanyuk, Fast Charge Transfer across the Li₇La₂Zr₂O₁₂ Solid Electrolyte/LiCoO₂ Cathode Interface Enabled by an
- Interphase-Engineered All-Thin-Film Architecture, ACS Appl. Mater. Interfaces 12 (32) (2020) 36196-36207.
- [75] A.L. Santhosha, L. Medenbach, J.R. Buchheim, P. Adelhelm, The Indium—Lithium Electrode in Solid-State Lithium-Ion Batteries: Phase Formation, Redox Potentials, and Interface Stability, Batter. Supercaps 2 (6) (2019) 524–529.
- [76] D. Carlier, L. Croguennec, G. Ceder, M. Menetrier, Y. Shao-Horn, C. Delmas, Structural study of the T $^\#$ 2-Li $_x$ CoO $_2$ (0.52 < x < or = 0.72) phase, Inorg. Chem. 43 (3) (2004) 914–922.